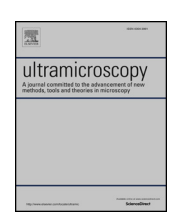
ELSEVIER

Contents lists available at ScienceDirect

Ultramicroscopy

journal homepage: www.elsevier.com/locate/ultramic



Investigating local oxidation processes in Fe thin films in a water vapor environment by *in situ* liquid cell TEM



Jordan W. Key^{a,*}, Shixiang Zhu^b, Christopher M. Rouleau^c, Raymond R. Unocic^c, Yao Xie^b, Josh Kacher^a

- ^a School of Materials Science and Engineering, Georgia Institute of Technology, Atlanta, GA, USA
- School of Industrial and Systems Engineering, Georgia Institute of Technology, Atlanta, GA, USA
- ^c Center for Nanophase Materials Science, Oak Ridge National Laboratory, Oak Ridge, TN, USA

ARTICLE INFO

Keywords: in situ TEM Oxidation Liquid cell TEM Image processing

ABSTRACT

Automated image recognition and analysis techniques were combined with liquid cell transmission electron microscopy to explore the oxidation kinetics of nanocrystalline Fe thin films in a water vapor environment. From $in\ situ$ microscopy experiments, localized oxidation was observed to initiate in the film then propagate in an unsteady fashion, alternatingly arresting and progressing. The oxidation front propagation occurred via new oxidation sites initiating 10s of nm ahead of the existing front rather than through a continuous expansion mechanism. The oxidation rate was seen to be highly dependent on electron dose rate, with increasing electron dose rate accelerating the oxidation front propagation and increasing the density of oxidation initiation sites. The $in\ situ$ experiments were also performed in diffraction space where it was seen that Fe_2O_3 was formed during oxidation. Coupling $in\ situ$ microscopy with automated image analysis creates new opportunities for studying the early stages of localized corrosion by providing direct observation of oxidation propagation as well as quantification of the oxidation rates and rapid identification of byproducts.

1. Introduction

Corrosion continues to be an important issue, affecting nearly every industry and costing the global economy an estimated \$2.5 trillion annually [1]. Due to the complexity of corrosion mechanisms and the difficulty in directly monitoring corrosion processes at relevant time and length scales, several fundamental processes that govern corrosion behavior remain unresolved. This is especially true for localized corrosion events, where the scale at which corrosion damage initiates, which is on the order of nanometers, and the rate at which corrosion fronts expand into the surrounding matrix make it difficult to determine corrosion initiation processes using conventional post mortem imaging alone [2]. Susceptibility to localized corrosion is known to be dependent on external environmental factors such as temperature and flow rates, surface conditions, and internal microstructural factors, including second phase distribution, grain boundary state, defect populations, and texture [2-4]. However, rapid expansion of the corrosion front from the initial attack site can obscure the direct identification of factors dictating the local susceptibility in post mortem analysis [3,5,6]. For example, work by Jain et al. investigating the corrosion of a sensitized Al-Mg alloy showed that the initiation of localized corrosion can trigger the spread of corrosion to the surrounding region, highlighting the importance of capturing the initial corrosion event [7].

Reports on the structural analysis of corrosion initiation and propagation behavior found in the literature generally rely on either high resolution post mortem analysis such as scanning electron microscopy of surface pit sites, or on in situ optical microscopy corrosion studies [8,9]. The characterized feature size in these optical studies (e.g. corrosion pit size or corrosion pathway) is limited to the micron domain or larger, obscuring the onset site of corrosion initiation. Electrochemical approaches to investigating corrosion behavior are often limited to bulkaverage behavior and do not provide direct insight into the locations of corrosion initiation and localized corrosion rates. Micro and nano capillary techniques provide only electrochemical behavior and not direct observation of the corrosion kinetics [10,11]. The influence of this lack of direct observation is readily apparent in the literature where conflicting reports on the influence of grain boundary character [12-14], grain size [15–19], dislocation content [20,21], local stress state [22], and orientation [23,24] can be found. For example, in ferrous systems specifically, some reports claim that reducing grain size increases corrosion resistance, while others claim that it reduces corrosion resistance instead [15,17]. A deeper understanding of corrosion initiation

^{*}Corresponding author at: Georgia Institute of Technology, Materials Science Department, 771 Ferst Dr. NW, Atlanta, GA 30313, United States. E-mail address: jkey9@gatech.edu (J.W. Key).

processes coupled with directly correlated microstructural analysis can help resolve these disagreements by identifying where, when, and how corrosion damage initiates and propagates through a material.

Liquid cell transmission electron microscopy (LC-TEM) is a characterization method that provides direct analysis of local material transformation and degradation events in aqueous or ambient-pressure gas environments at high spatial resolution such that microstructural features can be imaged/analyzed then correlated with corrosion behavior. In the LC-TEM approach, the sample of interest and liquid is encapsulated between Si chips with electron-transparent Si₃N₄ membranes, which facilitate direct observations of corrosion. The chips are hermetically sealed and liquid is flowed between the chips, protecting the surrounding vacuum condition of the TEM chamber, LC-TEM is seeing increasing use for diverse applications such as battery material degradation and nanoparticle synthesis and growth [25-28]. However, interpretation of the results gained through LC-TEM characterization can often be obscured when beam-driven effects are not properly accounted for, including the generation of radiolytic species, variations in local solution chemistry which drive changes in pH level, beam-induced heating, and charge transfer from the electron beam inducing potential gradients [29-31]. Radiolysis of the solvent can create species such as hydrogen radicals and solvated electrons that participate in the corrosion process near the beam [32]. Beam-induced heating has been shown to be small (a few degrees) under typical imaging conditions but can be more significant for more extreme dose rates [29,33]. Woehl et al. detailed various strategies for mitigating issues with sample preparation, film and window behavior, and beam effects [34]. For further detailed reading on corrosion studies using LC-TEM and beam-induced effects during such experiments, the reader is referred to the recent review by Song and Xie [32]. Studies on electron-irradiation of water vapor have shown that similar production of radiolytic species occurs in the vapor state, which can be used as the experimental environment rather than liquid [35].

A limited number of studies have applied LC-TEM to understanding localized corrosion processes both with and without potentiostatic control [30,36-40]. Schilling et al. investigate the influence of the electron beam on potentiostatic measurements and found that the beam current and liquid flow affect the open circuit potential measurements, though the beam-induced effects were found to reach equilibrium with time [36]. Park et al. investigated localized corrosion processes in a range of material/electrolyte systems with and without potentiostatic control and found that beam effects were minimal as long as low-dose protocols were followed [37]. Chee et al. characterized the localized pitting behavior of Al thin films in salt water environments with and without Au implantation and found that pitting events could be directly observed and correlated with ion-irradiated regions [30]. By observing the corrosion behavior of annealed and unannealed Fe thin films in acetic acid, Gross et al. showed that the corrosion resistance increased markedly with increasing grain size [38]. They also observed that corrosion attack occurred preferentially near abnormally grown grains, suggesting the influence of microgalvanic effects.

In this paper, we present results on dynamic observations of oxidation initiation and propagation events observed in nanocrystalline Fe thin films in a water vapor environment. The first section of the paper discusses qualitative observations of the oxidation processes. In the second section, we focus on the development of feature recognition and image analysis processes to characterize real- and diffraction-space structural and morphological changes during active oxidation events. This approach is motivated by the large increase in data collection rates associated with the transition from charged coupled device (CCD) electron detectors to complementary metal-oxide-semiconductor (CMOS) detectors, which enable higher electron sensitivity and significantly faster image collection rates [41].

2. Experimental methods

In this study, we investigated a model system of pure Fe corroded in a water vapor environment. Fe thin films, with thickness $\sim\!100\,\text{nm},$ were deposited directly onto the $\mathrm{Si}_3\mathrm{N}_4$ membrane in the bottom microchip of a liquid cell chipset using RF magnetron sputtering. A 99.99% purity Fe target (Kurt J. Lesker Co., Pittsburgh, Pennsylvania) was used as the source and sputtering was performed at a power of 75 W and a pressure of 5 mTorr for 30 min. The microstructure of the asdeposited thin films was characterized prior to exposure to any aqueous medium using bright-field (BF) and centered dark-field (CDF) TEM imaging, annular dark field scanning (S)TEM, and electron energy loss spectroscopy (EELS) analysis in a FEI Titan operated at 300 kV. The deposited film was observed to be stable under the electron beam under vacuum conditions

In situ observations of the oxidation process were made using a commercial liquid cell, with a chipset configured for a 500 nm liquid gap. (Protochips Inc., Morrisville, North Carolina). Prior to loading into the TEM to conduct experiments, the sample and tubing were flushed with deionized water to check the system for leaks. Experiments were conducted without any external liquid flow, examining oxidation in a water vapor environment under ambient pressure and temperature conditions. The vapor pressure was calculated to be approximately 3.5% using the Clausius-Clapeyron equation, though it should be noted that, with these experiments, the precise environment local to the film itself is difficult to determine. The oxidation events were captured using a Gatan OneView camera (Gatan Inc., Pleasanton, California) with video recording at 100 frames per second. Videos of the oxidation behavior were collected both in real space with the TEM operating in bright-field mode and in diffraction space with selected-area diffraction patterns acquired.

3. Results and discussion

3.1. Pre-oxidation characterization

Prior to conducting a leak check of the liquid cell holder, and thereby exposing the films to an aqueous environment, the microfluidic ports for the liquid cell holder were sealed and the films were characterized in terms of their initial structure and chemistry under vacuum conditions. BF and CDF TEM imaging showed that the initial film was uniform, with a grain size on the order of 10–20 nm (Fig. 1a–c). Microcracking is evident in the film (Fig. 1b), presumably due to

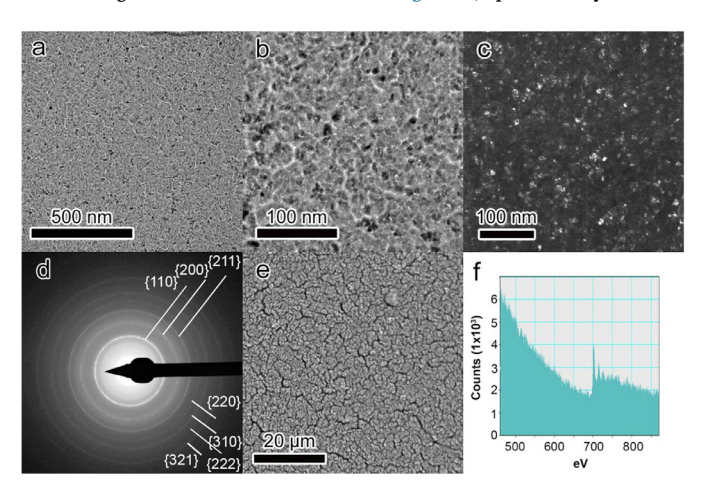


Fig. 1. BF TEM analysis of as-deposited Fe at a) low magnification and b) high magnification, c) CDF TEM image of a different region showing the distribution of nanograins, d) selected-area diffraction pattern collected from the film, and e) annular dark field STEM image. f) EELS analysis of as-deposited film showing Fe peak but no evidence of Fe oxides.

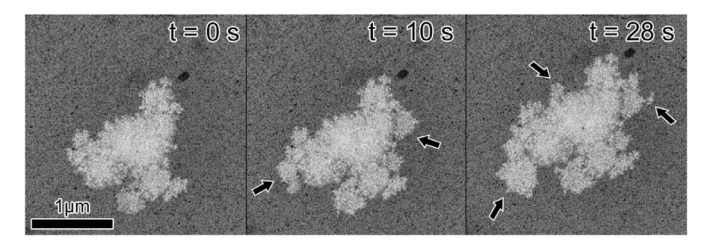


Fig. 2. Time sequence from bright-field TEM videos of an oxidation event, showing propagation of the oxidation front. Arrows indicate freshly oxidized regions.

interfacial stresses induced during the sputtering process between the Fe film and the $\mathrm{Si}_3\mathrm{N}_4$ membrane. These microcracks are more apparent in the annular dark field STEM image showed in Fig. 1e. Microcracks were not observed to have a strong influence on the oxidation initiation and propagation, possibly because the grain size is much smaller than the length scale of the microcracks. Selected-area diffraction patterns showed only solid rings, suggesting that the nanocrystalline film did not contain any strong texture components (Fig. 1d). EELS analysis did not reveal any significant Fe oxide presence prior to testing (Fig. 1f).

3.2. Qualitative analysis of oxidation in water vapor

Upon illuminating the sample with the electron beam, it was observed that the film quickly dewetted and oxidation initiated soon after. Fig. 2 is a series of bright-field images showing beam-accelerated oxidation of the Fe film after the liquid layer has dewetted. The corresponding video is in the Supplementary Information (Video 1). A region in the middle of the view field began to oxidize, accelerated by the irradiation of the electron beam, and the evolution of this oxidation event was recorded. As can be seen, the oxidation front expanded heterogeneously and sporadically from the existing oxidized region, with oxidation fronts initiating and arresting, consuming on the order of 10s of grains in that time. A new oxidation front would then initiate, either from the same location or another region of the previous front. The location of this reinitiation point could not be determined a priori. though the irregularity of the oxidation path suggests a microstructural influence. Further observation shows that the oxide is unstable, leading to dissolution of the material, suggesting a thin liquid layer may remain after exposure to the electron beam, although this could not be verified directly.

Fig. 3 shows an example of the oxidation front propagation at higher magnification. Here it can be seen that the oxidation propagation occurs by discrete jumps ahead of the existing front and then backfills in as the front catches up. The corresponding video can be found in the SI (Video 2). The reason for this behavior is currently unknown. It could be that these sites have some microstructural feature (e.g. grain boundary energy) or surface artifact that is more susceptible to the oxidation, making them easier initiation points. Then, as these sites dissolve, a sufficient amount of reactive species are created to facilitate the neighboring areas to be oxidized. However, without detailed information on the local microstructural characteristics, further

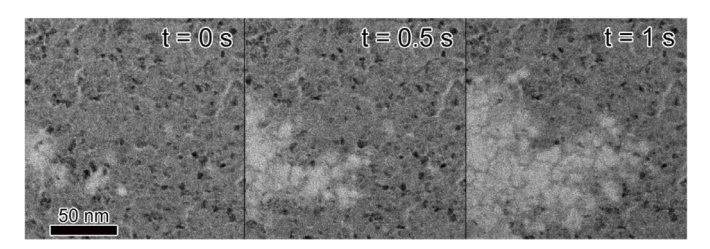


Fig. 3. Time sequence from bright-field video of an oxidation event showing discrete jump and backfill behavior of the oxidation front.

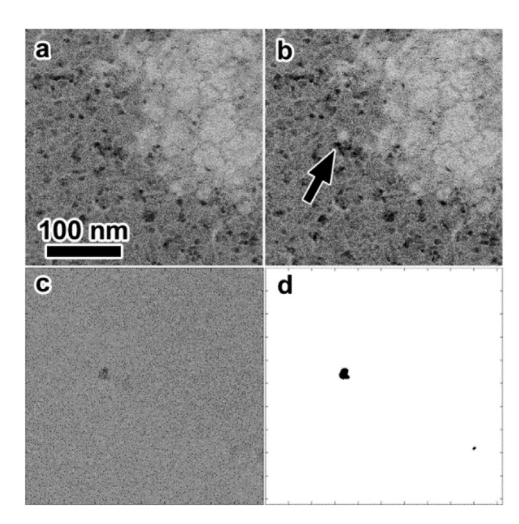


Fig. 4. Image analysis of a jump event during the oxidation front propagation: a) prior to jump event, b) highlighting the jump, c) image difference, and d) thresholded image difference. Frames a and b are separated by 0.01 s.

study will be required. Interactions of the electron beam with water molecules are known to generate positive and negative ions, free radicals, and excited molecules, resulting in changes in the environment chemistry and pH. These interactions have been shown to accelerate oxidation processes during LC-TEM observations in aqueous environments [30,38], and as radiolytic species can be generated during electron beam interactions with water vapor [35], we expect the electron beam to have a similar accelerating effect in this work.

3.3. Quantitative analysis of oxidation behavior

By taking an image difference between frames, the newly oxidized region can be isolated and, by filtering and thresholding the difference image, the exact area of the oxidized region determined. An example of this is shown in Fig. 4. Similar to what was seen in Fig. 3, the oxidation front propagated by a discrete jump. The analysis showed that, treating the problem as two-dimensional, 180 nm² was consumed by the jump, correlating to a diameter of approximately 15 nm. The similarity in size of the oxidized region and the average grain size suggests that the front propagation behavior is influenced by the film microstructure.

The type of analysis shown in Fig. 4 can be extended into an automated sequential thresholding routine, which allows entire video datasets to be rapidly analyzed to track the local oxidation rate and reveal the oxidation front morphology. In the automated process, the intensity of multiple images is averaged together and filtered using a lowpass-highpass filter to reduce noise. The image difference between a specified number of frames is taken and the resultant image difference is binarized using a fixed threshold value. The binarized image can be used to extract the total oxidized area as well as the current-frame oxidation rate. To further reduce noise effects, a minimum object size is set and all objects below this threshold that are detected as oxidized are filtered out.

This approach was used to investigate the influence of electron dose rate on the oxidation rate and behavior. In these experiments, the exact dose rate was not recorded, but it can be estimated using values from additional experiments at similar operating conditions. Two events at very different magnifications and dose rates were recorded: the higher dose rate event was on the order of $1500 \, \mathrm{e^- \ mm^{-2} \ s^{-1}}$ (Fig. 5a–d,i) and the lower dose rate event was approximately $500 \, \mathrm{e^- \ mm^{-2} \ s^{-1}}$ (Fig. 5e–h,j). Part of the analysis in Fig. 5 is shown in Video 3 of the SI for visualization. In Fig. 5, the accumulated newly oxidized area at two different times is shown for each magnification. Image processing parameters were optimized by manually comparing binarized images with the micrographs. In this case, 5 frames were averaged together,

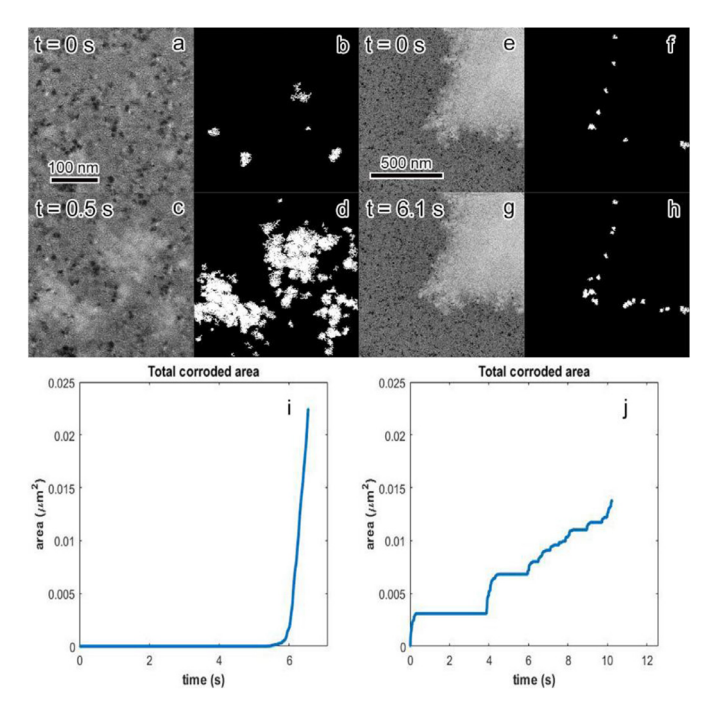


Fig. 5. Bright field images captured from video showing the initiation and expansion of the oxidation front for a higher dose rate event (a,c) and lower dose rate event (e,g). Associated binarized image differences showing the newly oxidized area over the 0.5 s time span (b,d) and the 6.1 s time span for the low dose rate (f,h). Total corroded area as a function of time for the higher dose rate event (i) and lower dose rate event (j) which shows arresting and reinitiation behavior that is not seen in the higher dose rate event.

and the image differences were taken 25 frames apart. As the image differencing only shows newly oxidized area, the upper-right portion of Fig. 5f and h, which was corroded prior to the start of observation, is not detected in the image differences and remains black. Only new oxidation events during observation appear in the analysis.

Clearly, the oxidation rate is higher at higher dose rate. The dose rate also seems to affect the sizes of the oxidation jump sites. The average size of the sites was measured by examining several frames of the difference images to find where jump sites occurred. The jump sites were defined for the lower dose rate case as the stable size of the oxidized area before the oxidation paused and reinitiated. Since the higher dose rate case did not exhibit pauses in the oxidation, the jump sites were given approximately one second to stabilize after first appearing before measurement. This was to ensure that an actual oxidation jump was occurring. For each case, several frames were examined to find ten jump sites to be measured and the average diameter was calculated. At the higher dose rate, the average diameter of the oxidation jump sites was approximately $19 \text{ nm} \pm 1 \text{ nm}$. As was the case in Fig. 3, this is

quite similar to the film grain size. However, at the lower dose rate, the size of the jump sites was slightly larger than the average grain size. During the experiment shown in Fig. 5e–h, the average diameter was approximately $27 \, \text{nm} \, \pm \, +3 \, \text{nm}$. Further investigation at more dose rates will provide additional insight to this effect.

In addition to allowing the size of the oxidation jump sites to be compared, this automated sequential thresholding also tracks the local oxidation rate. This can reveal differences in both kinetics and mechanisms, as shown in Fig. 5i and j. At the lower dose rate, the pattern of pausing and reinitiating (as in Fig. 2) is again observed. However, the higher dose rate event does not show this behavior but instead oxidizes steadily and more rapidly (about 20 times faster) than the lower dose rate case. Local beam-induced heating was not measured in these experiments but should have a negligible impact on the observed behavior. Thus we demonstrate that the type of analysis in Fig. 5i and j allows us to distinguish differences in both kinetics and oxidation behavior. To further investigate the quantitative effects of dose rate on oxidation initiation size and rate, additional experiments at a series of magnifications and recorded dose rates will be performed in a future study.

Observations were also made in diffraction space, providing insight into the crystallographic evolution of the film during the corrosion process. The beam was moved to an unoxidized area and recording of the diffraction patterns was initiated (Video 4 in the SI). The dose rate was on the order of that for the high dose rate event in Fig. 5 (on the order of $1500 \, {\rm e^- \ nm^{-2} \, s^{-1}}$). Image analysis of the diffraction patterns (Fig. 6) shows that the film is initially composed of polycrystalline Fe with no preferred texture. As the beam-accelerated corrosion process progressed, the sharpness of the diffraction rings decreased, suggesting a reduction in crystallinity; this is readily apparent from the loss of higher-order ring patterns in Fig. 6b. Signal detection algorithms can be used to isolate diffraction peaks from byproducts during the evolution of the film; however, it is often beneficial to have a narrow regime in which to search. The radial integration analysis described below is one way to refine the search field for signal detection.

Using approximately 1500 diffraction patterns corresponding to the dissolution event shown in Fig. 6, crystallographic evolution was tracked to extract information using a radial integration-based approach (Fig. 7). Fig. 7a shows the radial integration of the intensity of a diffraction pattern prior to the onset of oxidation, with peaks associated with diffraction from α -Fe clearly evident. This radial integration approach was automated and applied to all 1500 diffraction patterns, providing a quantification of the diffraction peak intensity as a function of diffraction angle (i.e. radius) and time. The variance of the diffraction intensity as a function of radius across the entire event was calculated and is plotted in Fig. 7b. Physically, this plot identifies diffraction angles at which the largest changes occur during the corrosion process. As can be seen, Bragg angles associated with α -Fe appear the largest in the plot, indicative of the dissolution process evident in Fig. 6. The background intensity, which undergoes little change over the dissolution

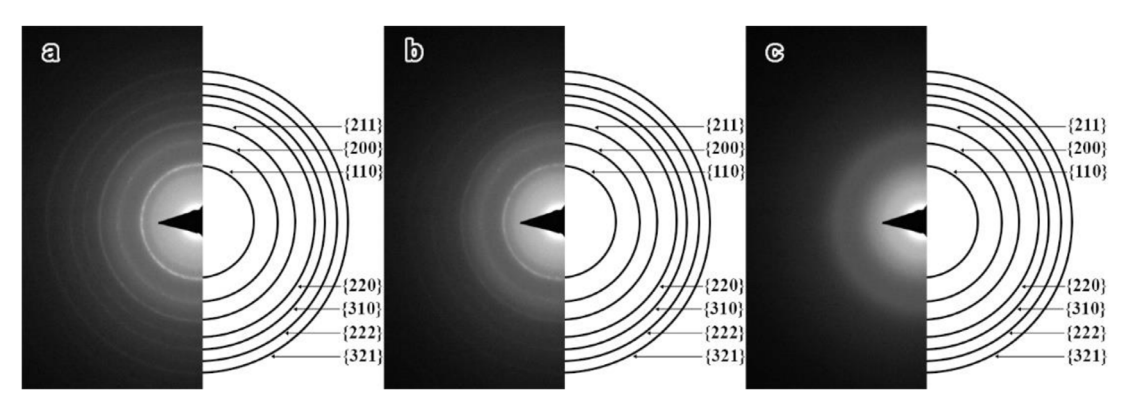
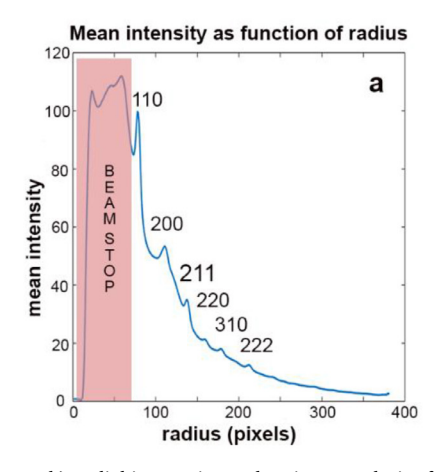
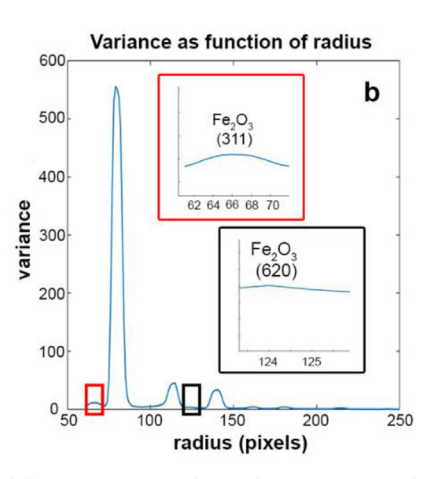


Fig. 6. Time sequence of diffraction patterns at t = 23 s (a), 26 s (b), and 33 s (c), showing phase change at one location as the corrosion proceeds.





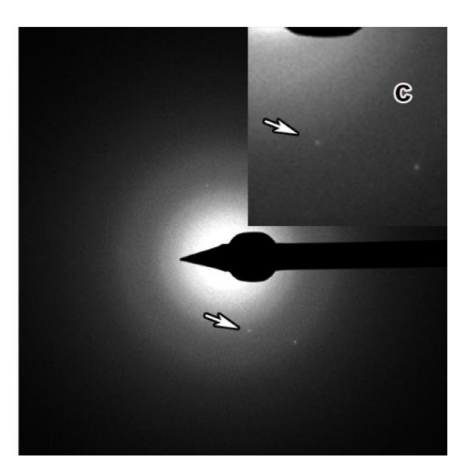


Fig. 7. a-b) Radial integration and variance analysis of diffraction pattern evolution during corrosion. The six peaks corresponding to the first six Fe Bragg peaks are labeled in the mean intensity plot (a). Closer inspection of two points of the variance plot is shown in (b). The leftmost peak (red box) is shown in the upper left inset, labeled as the (311) peak of Fe_2O_3 . The right peak (black box) is shown in the lower right inset, labeled as the (620) peak of Fe_2O_3 . CSAD pattern highlighting the diffraction spot associated with Fe-oxide. The spot marked by the arrow corresponds to (421) in Fe_2O_3 . (For interpretation of the references to colour in this figure legend, the reader is referred to the web version of this article.)

process, appears flat. Closer inspection of the variance plot can reveal information that is difficult to extract from the mean intensity plot. In this case, two subtle peaks were identified that corresponded to expected spacings for either Fe_2O_3 or Fe_3O_4 (Fig. 7b). The diffraction signal for these oxides are not readily apparent from Fig. 6, showing the usefulness of the above analysis.

Fig. 7c shows the diffraction peak pattern which contributed to the peak in the variance plot associated with Fe-oxide. This peak was identified using a sequential adaptive change-point detection algorithm in the radial range identified in the variance plot, the details of which can be found here [42]. The diffraction spot marked by the arrow was identified unambiguously at corresponding to the (421) peak in Fe₂O₃. However, the spot not marked by an arrow could be the (533) peak in either Fe₂O₃ or Fe₃O₄ (the difference is sub-angstrom). This confirms that Fe₂O₃ is a byproduct in the experiment but does not rule out the possible presence of Fe₃O₄. This highlights the importance of combining both radial intensity analysis with signal detection algorithms to identify the reaction byproducts. Radial intensity analysis alone may not be able to make unambiguous identification, but it can narrow down the field to reduce the load for the signal detection.

4. Conclusion

The results presented here show the developing use of *in situ* liquid cell electron microscopy to study oxidation in water-vapor environments, as well as the need for automated image analysis routines to extract the maximum information from the large data sets created by such experiments. Specific observations include:

- The electron dose rate had a significant impact on the oxidation rate, with higher dose rate leading to more rapid oxidation.
- The electron dose rate influenced the oxidation behavior, with the low dose rate events exhibiting a pattern of pausing and resuming whereas the high dose rate events exhibited steady oxidation.
- Radial integration analysis was used to refine the search field for a sequential adaptive change point algorithm that identified diffraction peaks associated with corrosion byproduct.

By coupling high-speed imaging and specialized liquid cell TEM holders, it is possible to obtain information on local oxidation rates, oxidation behavior, and byproducts. This holds great promise for developing the understanding of local corrosion processes. Future opportunities could include extending the analysis to track the fractality of the oxidation front, which is of interest in cellular automata

modeling [43,44]. The possibility of using scanning nanobeam diffraction [45] or precession electron diffraction [46] in combination with liquid cell to provide more localized diffraction information and more direct correlation with local microstructure is also promising [40].

Acknowledgments

We gratefully acknowledge funding from the US Office of Naval Research under Grant No. N00014-17-1-2646. A portion of this work was completed using support from the Institute of Materials at Georgia Tech. The film deposition and *in situ* TEM corrosion experiments were conducted at Oak Ridge National Laboratory's Center for Nanophase Materials Sciences (CNMS), which is a U.S. Department of Energy, Office of Science User Facility. Water vapor pressure calculations were performed by Dr. Kinga A. Unocic.

Supplementary materials

Supplementary material associated with this article can be found, in the online version, at doi:10.1016/j.ultramic.2019.112842.

References

- [1] G. Koch, et al., NACE International IMPACT Report, (2016).
- [2] G. Frankel, Pitting corrosion of metals a review of the critical factors, J. Electrochem. Soc. 145 (6) (1998) 2186–2198.
- [3] Z. Szklarska-Smialowska, Pitting corrosion of aluminum, Corros. Sci. 41 (9) (1999) 1743–1767.
- [4] E. Mostaed, et al., Microstructure, texture evolution, mechanical properties and corrosion behavior of ECAP processed ZK60 magnesium alloy for biodegradable applications, J. Mech. Behav. Biomed. Mater. 37 (2014) 307–322.
- [5] R. Foley, Localized corrosion of aluminum alloys—a review, Corrosion 42 (5) (1986) 277–288.
- [6] E. Ghali, W. Dietzel, K.-U. Kainer, General and localized corrosion of magnesium alloys: a critical review, J. Mater. Eng. Perform. 13 (1) (2004) 7–23.
- [7] S. Jain, et al., Spreading of intergranular corrosion on the surface of sensitized Al-4.4 Mg alloys: a general finding, Corros. Sci. 59 (2012) 136–147.
- [8] A. Pardo, et al., Corrosion behaviour of magnesium/aluminium alloys in 3.5 wt.% NaCl, Corros. Sci. 50 (3) (2008) 823–834.
- [9] R. Ambat, N.N. Aung, W. Zhou, Evaluation of microstructural effects on corrosion behaviour of AZ91D magnesium alloy, Corros. Sci. 42 (8) (2000) 1433–1455.
- [10] M. Breimesser, et al., Application of the electrochemical microcapillary technique to study intergranular stress corrosion cracking of austenitic stainless steel on the micrometre scale, Corros. Sci. 55 (2012) 126–132.
- [11] H. Krawiec, et al., The use of microcapillary techniques to study the corrosion resistance of AZ91 magnesium alloy at the microscale, Corros. Sci. 53 (10) (2011) 3108–3113.
- [12] V.Y. Gertsman, S.M. Bruemmer, Study of grain boundary character along intergranular stress corrosion crack paths in austenitic alloys, Acta Mater. 49 (9) (2001)

- 1589-1598.
- [13] R. Ishibashi, et al., Effect of grain boundary character distribution on stress corrosion cracking behavior in austenitic stainless steels, Materials Science Forum, Trans Tech Publ., 2005.
- [14] H. Kokawa, et al., Grain boundary engineering for intergranular corrosion resistant austenitic stainless steel, Key Engineering Materials, Trans Tech Publ., 2004.
- [15] V. Afshari, C. Dehghanian, Effects of grain size on the electrochemical corrosion behaviour of electrodeposited nanocrystalline Fe coatings in alkaline solution, Corros. Sci. 51 (8) (2009) 1844–1849.
- [16] B. Hadzima, et al., Microstructure and corrosion properties of ultrafine-grained interstitial free steel, Mater. Sci. Eng. 462 (1–2) (2007) 243–247.
- [17] M. Hasegawa, M. Osawa, Corrosion behavior of ultrafine grained austenitic stainless steel, Corrosion 40 (7) (1984) 371–374.
- [18] Y. Li, F. Wang, G. Liu, Grain size effect on the electrochemical corrosion behavior of surface nanocrystallized low-carbon steel, Corrosion 60 (10) (2004) 891–896.
- [19] A. Nikfahm, et al., Effect of grain size changes on corrosion behavior of copper produced by accumulative roll bonding process, Mate. Res. 16 (6) (2013) 1370–1386
- [20] J.G. Brunner, et al., Localized corrosion of ultrafine-grained Al–Mg model alloys, Electrochim. Acta 55 (6) (2010) 1966–1970.
- [21] M. Talianker, B. Cina, Retrogression and reaging and the role of dislocations in the stress corrosion of 7000-type aluminum alloys, Metall. Trans. A 20 (10) (1989) 2087–2092
- [22] B. Lu, H. Yu, J. Luo, Effects of plastic deformation and carbon dioxide on corrosion of pipeline steel in near-neutral pH groundwater, J. Mater. Eng. Perform. 22 (5) (2013) 1430–1435.
- [23] P.T. Brewick, et al., Microstructure-sensitive modeling of pitting corrosion: effect of the crystallographic orientation, Corros. Sci. 129 (2017) 54–69.
- [24] Q. Jiang, et al., Anisotropy of the crystallographic orientation and corrosion performance of high-strength AZ80 Mg alloy, J. Magn. Alloys 3 (4) (2015) 309–314.
- [25] M. Gu, et al., Demonstration of an electrochemical liquid cell for operando transmission electron microscopy observation of the lithiation/delithiation behavior of Si nanowire battery anodes, Nano Lett. 13 (12) (2013) 6106–6112.
- [26] R.L. Sacci, et al., Direct visualization of initial SEI morphology and growth kinetics during lithium deposition by in situ electrochemical transmission electron microscopy, Chem. Commun. 50 (17) (2014) 2104–2107.
- [27] A.V. Ievlev, et al., Quantitative description of crystal nucleation and growth from in situ liquid scanning transmission electron microscopy, ACS Nano 9 (12) (2015) 11784–11791.
- [28] S.A. Canepa, et al., Influence of cetyltrimethylammonium bromide on gold nanocrystal formation studied by in situ liquid cell scanning transmission electron microscopy, J. Phys. Chem. C 122 (4) (2018) 2350–2357.

- [29] N. de Jonge, F.M. Ross, Electron microscopy of specimens in liquid, Nat. Nanotechnol. 6 (2011) 695.
- [30] S.W. Chee, et al., Studying localized corrosion using liquid cell transmission electron microscopy, Chem. Commun. 51 (1) (2015) 168–171.
- [31] F.M. Ross, Opportunities and challenges in liquid cell electron microscopy, Science 350 (6267) (2015).
- [32] Z. Song, Z.-H. Xie, A literature review of *in situ* transmission electron microscopy technique in corrosion studies, Micron 112 (2018) 69–83.
- [33] J.M. Grogan, et al., Bubble and pattern formation in liquid induced by an electron beam, Nano Lett. 14 (1) (2014) 359–364.
- [34] T.J. Woehl, et al., Experimental procedures to mitigate electron beam induced artifacts during in situ fluid imaging of nanomaterials, Ultramicroscopy 127 (2013) 53–63.
- [35] C.E. Melton, Radiolysis of water vapor in a wide range radiolysis source of a mass spectrometer. I. Individual and total cross sections for the production of positive ions, negative ions, and free radicals by electrons, J. Phys. Chem. 74 (3) (1970) 582–587.
- [36] S. Schilling, et al., Practical aspects of electrochemical corrosion measurements during in situ analytical transmission electron microscopy (TEM) of austenitic stainless steel in aqueous media, Microsc. Microanal. 23 (4) (2017) 741–750.
- [37] J.H. Park, et al., In situ EC-TEM studies of metal thin film corrosion in liquid solutions at elevated temperatures, Microsc. Microanal. 24 (S1) (2018) 254–255.
- [38] D. Gross, et al., In situtem observations of corrosion in nanocrystalline Fe thin films, Process., Propert., Des. Adv. Ceram. Compos. II 261 (2016) 327–338.
- [39] S.W. Chee, et al., Metastable structures in Al thin films before the onset of corrosion pitting as observed using liquid cell transmission electron microscopy, Microsc. Microanal. 20 (2) (2014) 462–468.
- [40] S.C. Hayden, et al., Localized corrosion of low-carbon steel at the nanoscale, Npj Mater. Degrad. 3 (1) (2019) 17.
- [41] S.W. Chee, et al., Capturing dynamics in liquids with high-speed CMOS camerasopportunities and challenges, Microsc. Microanal. 23 (2017) 860–861 S1.
- [42] Y.Z. Cao, S. Zhu, Y. Xie, J. Key, J. Kacher, R.R. Unocic, C.M. Rouleau, Sequential Adaptive Detection For In-Situ Transmission Electron Microscopy (TEM), (2017) arXiv preprintarXiv:1710.11297..
- [43] J. Stafiej, D. di Caprio, Ł. Bartosik, Corrosion-passivation processes in a cellular automata based simulation study, J. Supercomput. 65 (2) (2013) 697–709.
- [44] C. Vautrin-Ul, et al., Numerical simulations of spatial heterogeneity formation in metal corrosion, Corros. Sci. 50 (8) (2008) 2149–2158.
- [45] C. Gammer, et al., Diffraction contrast imaging using virtual apertures, Ultramicroscopy 155 (2015) 1–10.
- [46] J.G. Brons, G.B. Thompson, Orientation mapping via precession-enhanced electron diffraction and its applications in materials science, JOM 66 (1) (2014) 165–170.